Suppression of cavitation in melted tungsten by doping with lanthanum oxide

2014 Nucl. Fusion 54 083026

(http://iopscience.iop.org/0029-5515/54/8/083026)

IOP Publishing | International Atomic Energy Agency Nuclear Fusion
Nucl. Fusion **54** (2014) 083026 (9pp) doi:10.1088/0029-5515/54/8/083026

Suppression of cavitation in melted tungsten by doping with lanthanum oxide

Y. Yuan[1,2], B. Xu[2], B.Q. Fu[2], H. Greuner[3], B. Böswirth[3], H.Y. Xu[2], C. Li[2], Y.Z. Jia[2], S.L. Qu[2], G.-N. Luo[4], G.H. Lu[1] and W. Liu[2]

[1] School of Physics and Nuclear Energy Engineering, Beihang University, Beijing 100191, People's Republic of China
[2] School of Material Science and Engineering, Tsinghua University, Beijing 100084, People's Republic of China
[3] Max-Planck-Institute for Plasma Physics, Boltzmannstr. 2, 85748 Garching, Germany
[4] Institute of Plasma Physics, Chinese Academy of Sciences, Hefei, Anhui 230031, People's Republic of China

E-mail: liuw@mail.tsinghua.edu.cn and yueyuan@buaa.edu.cn

Received 25 January 2014, revised 15 May 2014
Accepted for publication 30 May 2014
Published 26 June 2014

Abstract

Melting and boiling behaviour of pure tungsten and 1 wt% lanthanum-oxide-doped tungsten (WL10) are investigated, focusing on the material selection with respect to material loss induced by cavitation. Melting experiments under high heat loads are carried out in the high heat flux facility GLADIS. Pulsed hydrogen neutral beams with heat flux of 10 and 23 MW m^{-2} are applied onto the adiabatically loaded samples for intense surface melting. Melt layer of the two tungsten grades exhibit different microstructure characteristics. Substantive voids owning to cavitation in the liquid phase are observed in pure W and lead to porous resolidified material. However, little cavitation bubbles can be found in the dense resolidified layer of WL10. In order to find out the gaseous sources, vapour collection is performed and the components are subsequently detected. Based on the observations and analyses, the microstructure evolutions corresponding to melting and vapourization behaviour of the two tungsten grades are tentatively described, and furthermore, the underlying mechanisms of cavitation in pure W and its suppression in WL10 are discussed.

Keywords: tungsten, melting, cavitation, WL10, high heat flux

(Some figures may appear in colour only in the online journal)

1. Introduction

Material selection for the plasma-facing materials (PFMs) is of great importance for the plasma–wall interaction (PWI) which is a serious concern for next step fusion reactors. Tungsten (W) with high melting point, high thermal conductivity, low tritium retention and low sputtering yield is chosen as divertor PFM of ITER and the most promising candidate material for the first wall in DEMO and fusion reactors beyond.

However, one of the main constraints of W consists in the probability of melting under high heat loads under uncontrolled operating conditions such as disruptions (20–100 MJ m^{-2} with duration 0.1–10 ms), vertical displacement events (VDEs, ~60 MJ m^{-2} with duration 100–300 ms), edge-localized modes (ELMs, ~1–3 MJ m^{-2} with duration 0.1–1 ms) as well as leading edges due to target misalignments [1–3]. The associated melt layer motion and ejection leading to material redistribution and macroscopic loss significantly threaten the lifetime of W-PFMs [4–6]. Melt ejection, especially, has recently gained increasing attentions, since it not only causes substantial material erosion but also can finally contaminate the plasma and seriously deteriorate the plasma operation [7–10]. Volume bubble boiling (cavitation) inside the melt layer is considered as one of the mechanisms for melt ejection: bubbles form and grow in the superheated melt layer, and then burst when they meet the melt layer surface, simultaneously inducing the ejection of liquid droplets [11, 12]. The physics of cavitation has been described using computational fluid dynamics simulations [12]. Nevertheless, the mechanism of cavitation in W melt is not experimentally revealed as yet [7, 8, 13, 14].

W melting under plasma impact is notoriously difficult to be inhibited, since possible loss of plasma control cannot be excluded in actual operations. From the material research and development point of view, improvements are indispensable to reduce the risks induced by cavitation. Some attempts have been made in Coenen *et al* 's work [8] to control the material erosions under high heat flux (HHF) conditions: (1) improving W purity, and however cavitation still occurs when the purity goes to 99.9999%; (2) alloying, i.e. W–Ta, but it turns out

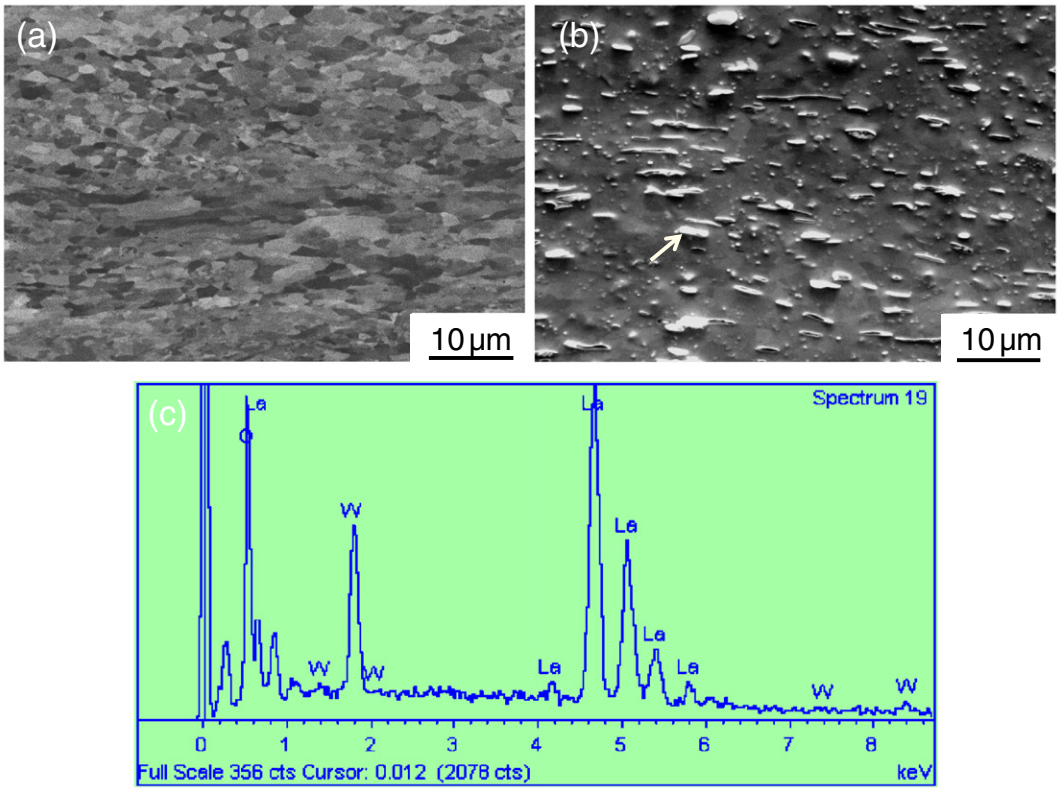

Figure 1. Microstructure on the transverse section of the original (*a*) CPW and (*b*) WL10. (*c*) EDX result for a dispersed particle (indicated by an arrow) in (*b*).

that cavitation and W spraying get much stronger. Besides, doping with rare-earth oxides, e.g. La_2O_3, is another way for W improvement [15, 16]. Although melting experiments were performed on W–La_2O_3 in many previous investigations [17–19], phenomena on cavitation were rarely concerned. Recently, we have investigated the melting behaviour of W–1 wt% La_2O_3 and found that the cavitation are significantly mitigated [13]. However, the detailed process and mechanism of the suppression of cavitation need to be further clarified.

In this study, melting and boiling behaviour of pure and lanthanum doped tungsten under a single HHF load is comparatively investigated in the frame of cavitation issues. Detailed characteristics of melt layer structure are analysed. Gaseous sources are indirectly investigated with aid of the collection of the vapour deposits. According to the experimental results, the possible underlying mechanisms of cavitation in pure tungsten and its suppression in lanthanum doped tungsten under high heat loads are discussed.

2. Experimental

The materials used in this work are commercial-purity tungsten (CPW) with a purity of >99.9 wt% and W–1 wt% La_2O_3 (WL10). They are respectively provided by Advanced Technology & Materials CO, Ltd and Beijing Tian-Long Tungsten & molybdenum CO, Ltd in China. They are produced from high-purity powder by cold isostatic pressing, sintering, under hydrogen atmosphere, and finally rolled with a reduction about 85% to a thickness of ~3 mm. The relative densities of the rolled CPW and WL10 are 98.5% and 98.1% respectively. Figure 1 shows a heavily deformed microstructure on the transverse section of the as-received CPW and WL10. Their average grain sizes are similar, on the order of 5 μm. For the original WL10 (figures 1(*b*) and (*c*)), La_2O_3 particles dispersed in the W matrix and some big ones are significantly elongated to plate-like structure after rolling deformation.

Melting experiments are carried out in the HHF test facility GLADIS (Garching LArge DIvertor Sample test facility) at IPP-Garching [20]. Hydrogen neutral beams are used for applying the heat fluxes. The diameter of the Gaussian beam at 80% central heat flux is 70 mm. Test samples with the dimensions of 80 × 65 × 3 mm^3 are mounted on carbon fibre reinforced composite (CFC) sample holders which are fastened on a cooling tube on the rear side. Thermal radiation is the key contributor, especially at high temperatures without melting, to the cooling of the adiabatically loaded sample [21]. The incident beam perpendicularly loads on the sample surface which is inclined at 82° to the horizontal. An IR camera (10 frames s^{-1}, 10 μm wave length) is employed to record the real-time macro-morphology changes due to surface melting.

Heat loading with central heat flux of 23 MW m^{-2} and duration of 1.8 s (~41.4 MJ m^{-2}) is performed to obtain severe surface melting, according to our pervious melting tests [13], for investigating the characteristics of molten layer in great detail. The corresponding mean energy and flux of hydrogen particles are ~22 keV and 6.6 × 10^{21} $m^{-2}s^{-1}$ respectively, which can cause a local beam pressure ~20 Pa on the loaded surface. Because a vapour cloud is expected to be formed around the exposed area when melting

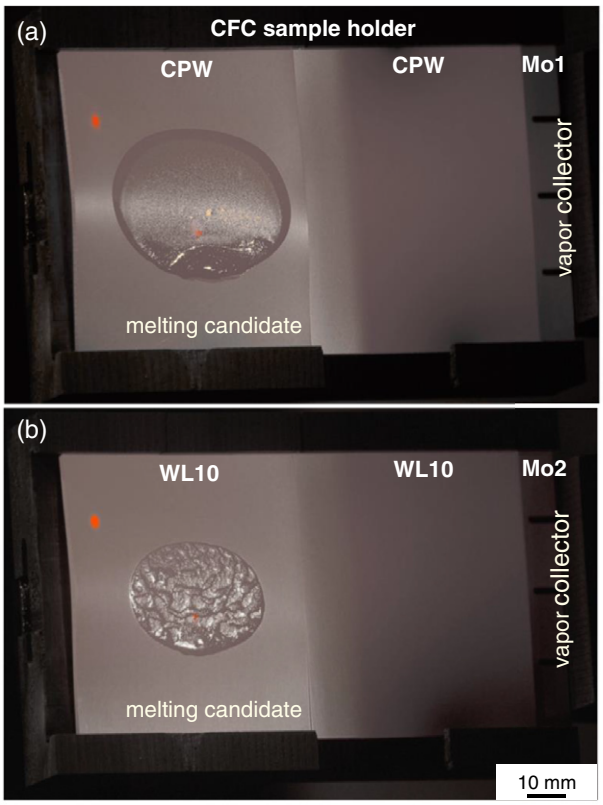

Figure 2. Photographs of samples fixed on CFC sample holders. Melting samples are (*a*) CPW and (*b*) WL10, and the corresponding vapour collectors are (*a*) Mo1 and (*b*) Mo2, respectively.

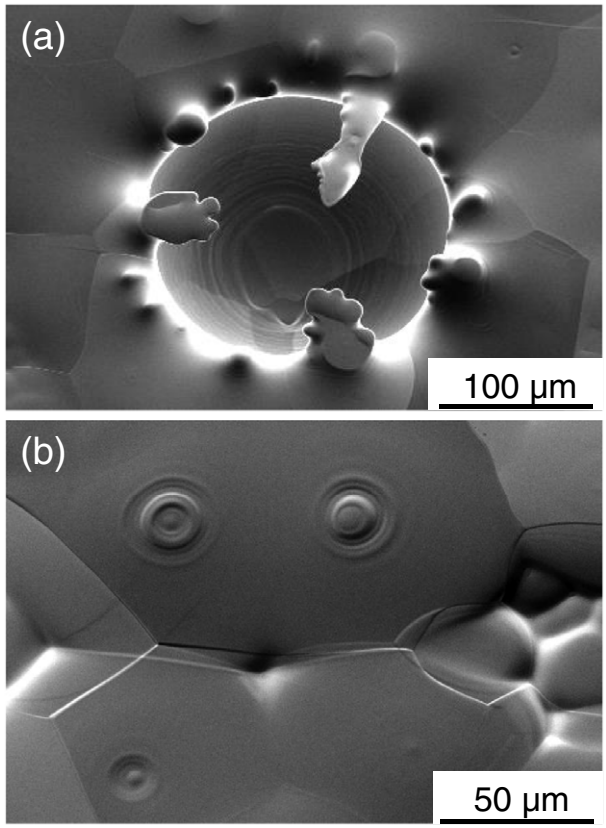

Figure 3. Surface morphology of the CPW melt area exposed to 23 MW m^{-2} for 1.8 s: (*a*) a big open bubble, (*b*) droplets redeposit on the surrounding melt layer surface.

and vapourization/boiling occurs [11], we conduct vapour collection experiments to find out the vapourization/boiling source (details of the vapour collection experiments will be described hereafter). In order to slow down the melting and vapourization process for better vapour gathering, the heat flux is adjusted to a lower value of 10 MW m^{-2} and the pulse duration set as 4.5 s (~45 MJ m^{-2}). In this case, the mean energy of hydrogen particles is ~15 keV and the flux is also around 4×10^{21} m^{-2}s^{-1}, and the corresponding beam pressure is close to ~10 Pa. For vapour collection, particularly, test samples are placed as shown in figure 2. The beam centre is located at the centre of the left one for melting (melting candidate), a molybdenum plate (collector) is put nearby for vapour deposition. To avoid the melting of Mo-collector during heat loading, the collector is fixed far away from the beam centre (>90 mm). Another piece of CPW/WL10 plate is inserted between the melting candidate and collector to protect the CFC sample holder from exposure, and hence reduce the contamination from carbon ablation. The corresponding vapour collectors are labelled as Mo1 and Mo2 for CPW and WL10, respectively. It is worth noting that the melting test is first performed on WL10, and successively on CPW with the same sample holder.

Surface morphologies and cross-sectional microstructures are investigated by scanning electron microscope (SEM). Various component analyses, i.e. energy dispersive x-ray spectrometry (EDX), electron probe microanalysis (EPMA), inductive-coupled plasma atomic-emission spectrometry (ICP) and x-ray photoelectron spectroscopy (XPS) were appropriately implemented.

3. Results

After 1.8 s heat loading at 23 MW m^{-2}, both of the CPW and WL10 severely melt and big melt areas are formed. According to the thermograms recorded by the IR camera, surface melting starts from the sample centre at around 1.5 s for CPW, and a little bit earlier (<0.1 s) for WL10. The onsets of melting for both tungsten grades here are consistent with the ones obtained in the previous tests [13] under the same experimental setup, indicating the good repeatability of our tests. Hence, the sample centres suffer a melting duration of ~0.3 s in the 1.8 s loading. Aiming at the study of the melting and boiling behaviour, herein, we focus on the local microstructure evolution of the melt layer around the loading centre.

Surface morphology in the centre of the CPW melting sample after exposure to 23 MW m^{-2} for 1.8 s is shown in figure 3. The most striking feature is the big hemispherical hole (figure 3(*a*)). It indicates that a spherical gas bubble is formed in the liquid phase and then bursts on the free liquid surface. Other noticeable features such as melt debris around the hole, ripples on the inner wall of the hole (figure 3(*a*)) and ripple-rings on the surrounding melt layer surface (figure 3(*b*)) are believed to be closely linked to the bubble bursting [12, 22–24]. Bubble bursting starts with rupture of the top wall of the bubble. Some part of the thin film ejects outwards as tiny droplets and

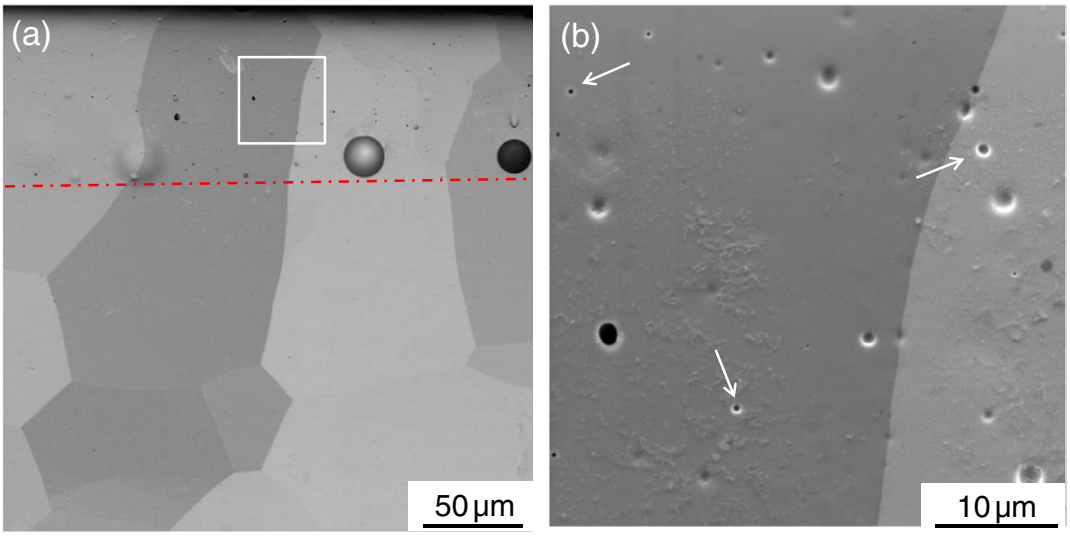

Figure 4. (*a*) Cross-section of the CPW melt layer after exposure to 23 MW m^{-2} for 1.8 s. The red dotted line indicates the boundary where intense boiling starts. (*b*) Magnification of the white rectangle area in (*a*).

the rest part snaps back resulting in the melt debris around the bubble crater. Subsequently, the submerged bubble wall converges on the centre and develops a jet to be ejected upwards from the bubble centre. The jet breaks into droplets and ejects outward, and the bottom portion snaps back which leads to disturbance of the liquid and finally results in the ripples on the bubble wall. The ejected droplets, arising from the disintegration of the top bubble wall and the breakup of the jet, redeposit and impact with the surrounding free liquid surface causing the ripple-rings. These subtle surface features, e.g. the ripples, surviving from the liquid–solid transition, imply that the melt layer resolidifies quite fast when the heat loading terminates. The observations on the surface of the CPW melt layer suggest that, under the applied heat load cavitation occurs in the CPW melt layer and concomitant bubble bursting induces droplets ejection.

Figure 4 presents the cross-section of the CPW melt layer after 23 MW m^{-2}, 1.8 s loading. We can see columnar grains ranged on the top surface and grains in the bulk strongly recrystallized (figure 4(*a*)). We speculate that the big columnar grains developing from the bulk to the top surface attribute to the epitaxial growth [25]. When the melt layer resolidifies, nucleation occurs by arranging atoms from the liquid metal upon the unmolten grains without altering their existing crystallographic orientations. Then they grow into columnar grains parallel to the cooling direction. In the upper part of the columnar grains, many big spherical voids or bubbles almost arrange in a line (indicated by a red dotted line). This phenomenon can also be found in resolidified tungsten in other references, e.g. figure 5 in [13] and figure 9(*c*) in [26]. The HHF loading generates a temperature gradient in the thickness direction. The big bubbles define a boundary where intense boiling starts, indicating the tungsten melt above this boundary (the red dotted line) is superheated. In this superheated layer, there are a lot of small spherical cavities as shown in figure 4(*b*), which correspond to the nuclei and initially growing bubbles. In principle, there is a molten to non-molten transition boundary close to the superheated melt

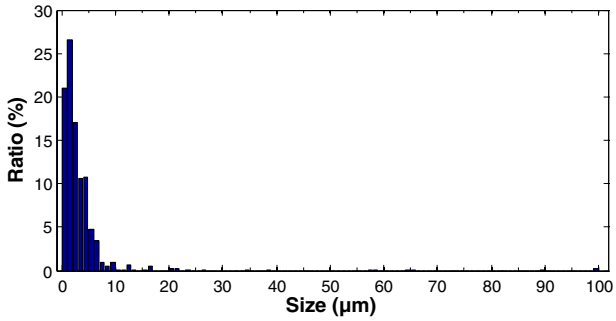

Figure 5. Size distribution of the voids in the resolidified layer of CPW after exposure to 23 MW m^{-2} for 1.8 s.

layer. But it is difficult to judge this transition boundary based on the crystallographic characteristics after resolidification. Consequently, for the sake of simplicity, we refer to the red dotted line as the molten to non-molten transition boundary. That is, only the part above the red dotted line is considered as molten/resolidified layer. We measure the sizes of the voids dispersed in the CPW resolidified layer, according to >10 cross-sectional views. The void size distribution is summarized in figure 5. The voids can be classified as two types: 'big voids' with size ranging from 5 μm to several tens of μm and 'small voids' with size $\leqslant 5$ μm. The number of the small voids is significantly higher compared to the big ones. However, the total area of the big voids is about 23 times larger than the small ones. It suggests that the big voids which are derived from big bubbles in the liquid phase can cause more serious harm to the resolidified layer. The resulting porosity of the resolidified layer is $\sim$8.6% which is defined as the sum area of the voids dividing by that of the resolidified layer. This kind of porous resolidified material can reduce the cracking resistance [8] and significantly degrade the power-handling capabilities [7].

Surface structures in the centre of the WL10 melt layer under the same heat loading are shown in figure 6. The raised

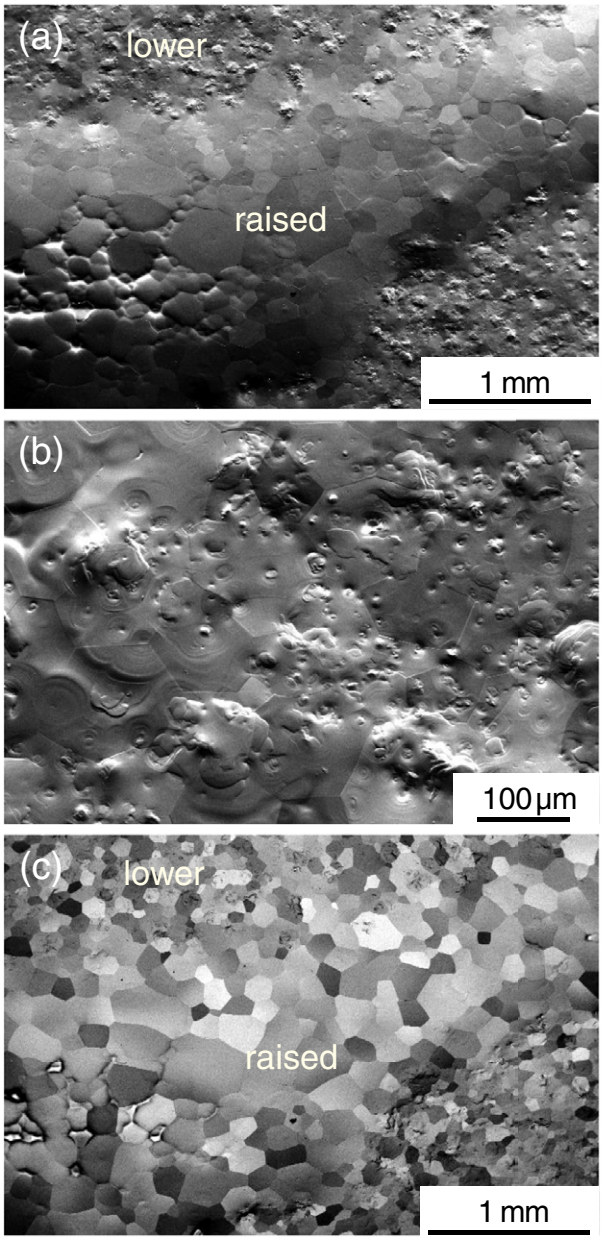

Figure 6. Surface structures of the WL10 melt area after loaded with 23 MW m^{-2} for 1.8 s: (*a*) SEM image of the undulating surface, (*b*) detailed surface morphology of the lower part, (*c*) BSE (back-scattered electron) image corresponding to (*a*).

and lower part of the undulating surface exhibit much different features. Surface is smooth for the raised part, and however, lots of small pits and local accumulations are found on the lower part (figures 6(*a*) and (*b*)). Grains are very big for the raise part, while they are relatively small for the lower part (figure 6(*c*)). To further understand these differences, the cross-sectional structures of the raised and lower part are observed and shown in figure 7. For the raised part (figure 7(*a*)), the dispersed particles are La_2O_3 validated by EPMA analysis (figure 7(*c*)). According to the features of La_2O_3 particles, the cross-section can be divided into three typical layers. In the layer I, where keeps a distance to the top surface, La_2O_3 particles maintain the plate-like structure as same as the situation before exposure (figure 1(*b*)) and the W grains are recrystallized. In the layer II, where gets closer to the top surface, La_2O_3 particles change to spherical shape. The W matrix includes larger recrystallized grains as well as the bottom of the columnar grains. In the layer III, the top part of the columnar grains, resulting from epitaxial growth [25], are quite compact. As shown in figure 7(*d*), La_2O_3 particles become much smaller (<0.5 μm). They are distributed in series of approximate lines, implying the movements in the W melt. Moreover, the content of La in the layer III is only 7.8 $\mu g\, g^{-1}$ detected by ICP. These provide convincing evidences that La_2O_3 particles are almost vapourized and leave a quasi-pure W melt layer on the top surface. Comparing figures 7(*a*) and (*b*), the main difference between the raised part and the lower part lies in the top quasi-pure W melt layer (layer III). We believe that the wave-like motion of the quasi-pure W melt layer accounts for such melt layer redistribution. The lower part, where loses the top quasi-pure W melt layer, exposes the inner layer II outside (figure 7(*b*)), and the dispersed La_2O_3 affects the surface morphology (figure 6(*b*)). We expect that the La_2O_3 particles in layer II would perform in the same way, namely being vapourized off substantially, under multiple heat loads. The raised part, where accumulates thick W melt layer, obtains big columnar grains with smooth surface (figures 6(*a*) and 7(*a*)). It also means that the layer III mainly represents the molten/resolidified layer for WL10.

Microstructures of the two tungsten grades after the same single heat loading described above illustrate that cavitation only occurs in the melt layer of CPW, while it is inhibited in WL10. Besides, for the 10 MW m^{-2}, 4.5 s loading, cavitation is also observed for CPW and suppressed for WL10. Since the resulting microstructures are analogous to the ones of 23 MW m^{-2}, 1.8 s loading, they are not shown here. Bubble intensely boiling and bursting on the CPW surface and release of the contained gas can increase the corresponding component in the vapour cloud above the sample surface. In contrast, this effect is negligible during WL10 melting. Therefore, it implies a possibility to confirm the gas component of bubbles in the CPW via comparing the components of vapour deposits on Mo1 and Mo2. Figure 8 presents the results of XPS analysis on the surface of Mo1 and Mo2. For Mo2, the amount of W is calculated to be 3.45 at% and La is 6.8 at%. For Mo1, W is significant increased to 35.2 at%. Meanwhile, a small amount of La (~1 at%) is detected. This should be ascribed to the order of the melting tests, i.e. WL10 followed by CPW: La-deposits on the sample holder and the surrounding components can pollute Mo1 during the following heat flux test. The XPS results indicate that W intensively vapourizes during CPW melting, and in contrast, W slightly vapourizes when WL10 melts. Combining the structure observations before, it is reasonable to conjecture that the bubbles in the CPW melt layer are W vapour bubble. In other words, cavitation in CPW is due to local boiling of W itself. In fact, corresponding to the gas pressure ~10–20 Pa during beam loading, the boiling temperature of W is up to 3900 K [27], just a little above the melting point (3695 K), and hence the boiling of W is reasonable.

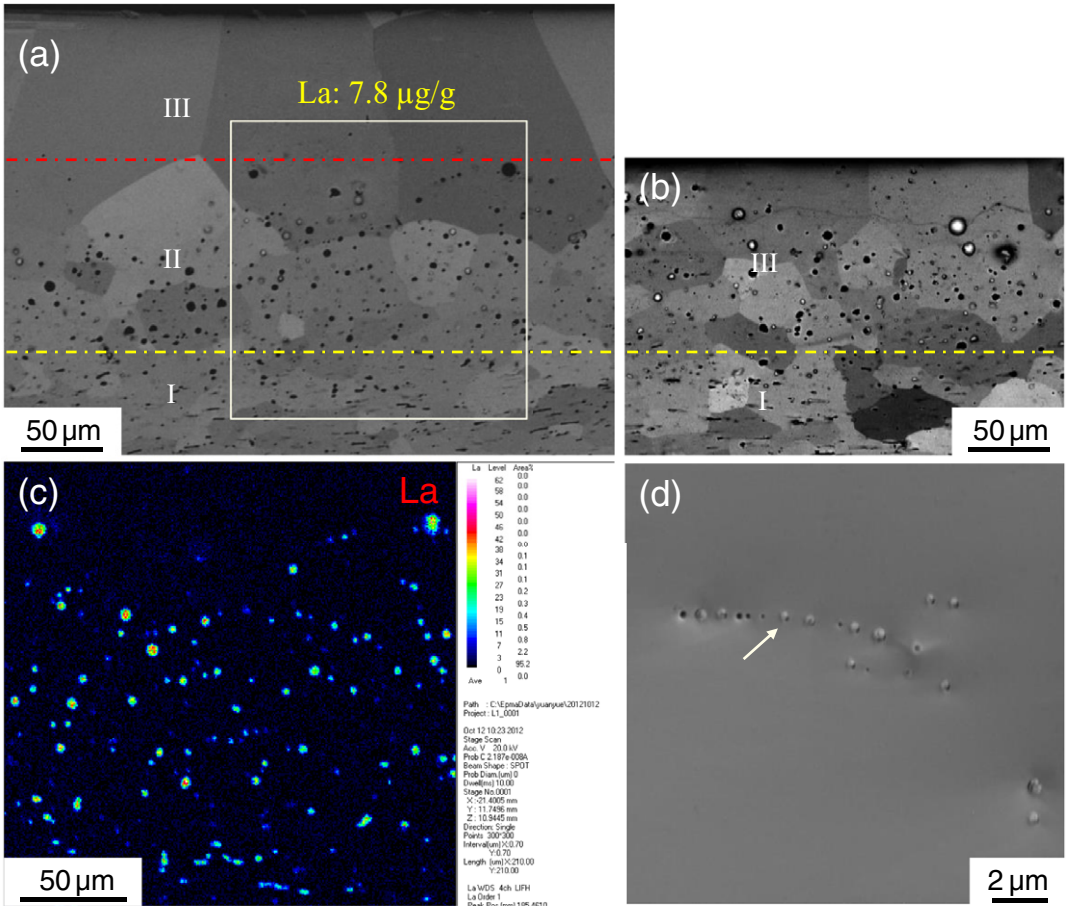

Figure 7. Microstructures on the cross-section of WL10 after 23 MW m^{-2} heat loading. (*a*) and (*b*) are BSE images corresponding to (*a*) raised part and (*b*) lower part of the WL10 melt, respectively. The content of La remained in the layer III is 7.8 $\mu g\, g^{-1}$ detected by ICP. (*c*) EPMA results of the square area in (*a*). (*d*) SEM image of the columnar grain in the top layer III, and some tiny La_2O_3 particles can be found.

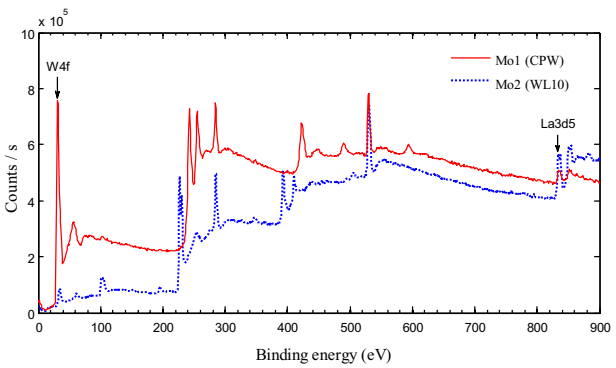

Figure 8. XPS results of the surface components of the vapour collectors Mo1 and Mo2 corresponding to the melting of CPW and WL10, respectively.

4. Discussion

Cavitation in the CPW melt layer is observed after the hydrogen neutral beam high heat load in the present work. The similar phenomenon also occurs in W under heat loads with electron beam or plasma impact [4, 7, 14, 28]. These experimental results indicate that cavitation in W mainly depends on the thermal response of the tungsten material itself and it has little relevance to the incident particles. Comparisons on the melt layer structures and vapour deposit components of CPW and WL10 show that cavitation is caused by the local boiling of the superheated W melt. An important concern here is heterogeneous bubble nucleation in the CPW melt layer. Preexisted gas/vapour clusters can act as bubble initiators when W melts and gets superheated [24]. The preexisted gas/vapour clusters are most likely derived from the impurities contained in the CPW. Indeed, W material cannot reach the state of absolute purity in the industrial production. Once the impurities exist, even extremely few, they can serving as nucleation sites for heterogeneous nucleation reduce the required nucleation superheat [29], and thus activate and enhance the W vapour bubble formation in the superheated W melt. It is also confirmed by the experiments in [8] which reported that cavitation was still found in an ultra-high purity W (99.9999%) under high heat loads. On the basis of the experimental results, we schematically describe the melting and boiling behaviour of W under high heat loads in figure 9. Impurities first vapourize and become vapor clusters under heat loading. With temperature increasing, W melts and gets superheated. Those preexisting impurity vapour clusters induce the heterogeneous nucleation of W vapour bubbles. Then the W vapour bubbles grow bigger and move upwards. Some of them burst on the top surface and discharge its vapour

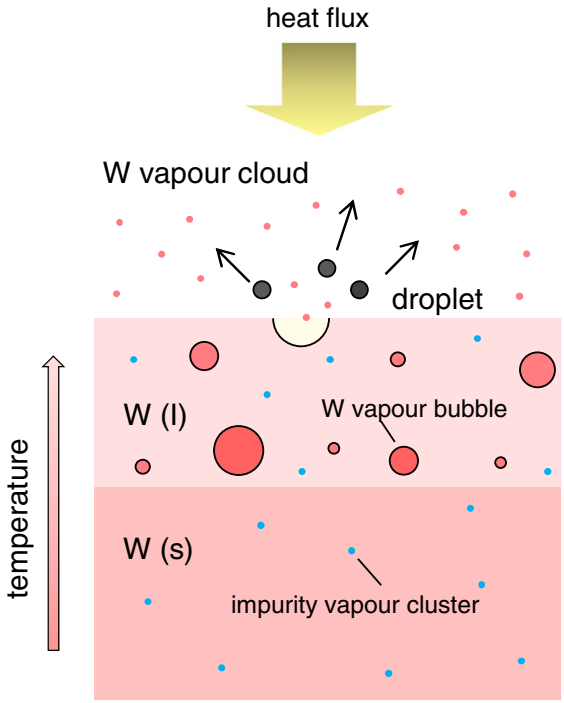

Figure 9. Schematic presentation of the melting and boiling behaviour of W under HHF load.

into the ambient, resulting in a dense W vapour cloud above the surface. Meanwhile, bubble bursting induces droplets ejection in the forms of disintegration of the top bubble wall and breakup of the developed jet as we discuss in section 3 (figure 3). It is important to point out that we do not take into account the incline of the sample and the resulting melt layer motion of the W melt layer, which little influence the crucial factors for the melting and boiling process.

The characteristics of WL10 after melting exposure summarized in section 3 point out that the thermal response of WL10 is closely correlated with the evolution of La_2O_3 particles. Typical features of WL10 under heat loading are shown as a schematic presentation in figure 10(*a*). Consistent with the experimental observations (figure 7), WL10 is divided into three layers. The top layer III is the W melt layer. So the temperatures of layer II and layer I are supposed to approach the melting point of W (3695 K). Hereinto, layer II which is next to the top melt layer is little hotter than layer I. It should be noted that the doped La_2O_3 can start transforming in two ways at low temperatures relative to the heated W matrix.

(1) Vapourization (>2300 K) by the reaction

$$La_2O_3(s) \rightarrow 2LaO(g) + \frac{1}{2}O_2(g), \quad (1)$$

and yielding $\Delta H_1 = 1.78\,\mathrm{MJ\,mol^{-1}}$ [30].

(2) Melting (>2586 K)

$$La_2O_3(s) \rightarrow La_2O_3(l), \quad (2)$$

and affording $\Delta H_2 \approx 0.18\,\mathrm{MJ\,mol^{-1}}$ [31, 32].

Therefore, La-gases will exist in the plate-like cavities once reaction (1) occurs (layer I). With increasing temperature, the vapour pressure of La-gases increases, and meanwhile the yield strength of the W matrix decreases [33]. As a result, the powerful La-gases derive the adjacent W matrix deformation and resulting in the spherical shape (layer II). As soon as the W matrix melts (layer III), the La-gases quickly run across the hot liquid layer and escape out leading to the formation of La-vapour cloud above the surface. Thus, the content of La in the layer III is sharply reduced as that described in section 3. These thermal processes finally make the WL10 become a gradient material due to the uneven distribution of La_2O_3 in the heat affected zone.

A dramatic phenomenon here is the suppression of cavitation in the melt layer III. According to the mechanism of W boiling in CPW, we propose two possibilities for the W boiling suppression owing to the addition of La_2O_3. The first one is 'cleaning effect' from the point of view of reducing/cleaning the potential nucleation sites for W vapour bubble formation, i.e. impurities: when the La-gases bubbles move in the liquid W (layer III), they swallow up the tiny impurity vapour clusters by coalescence and then bring them out from the W melt. This process is illustrated in the layer III in figure 10(*a*). The other possibility is 'cooling effect' as simply described in figure 10(*b*). In layer III, not only the transformations of La_2O_3 consume part of the heat ($\Delta H_1 + \Delta H_2$), but also the escape of hot La-gases takes energy from the melt, referred as Q_g. The energy, $Q_{La_2O_3} = \Delta H_1 + \Delta H_2 + Q_g$, is derived from the added La_2O_3. To rough estimate the cooling effect, we calculate the heat consumption of La_2O_3 in the top melt layer according to the dimensions shown in figure 7(*a*), and assume that: (1) the 1 wt% La_2O_3 in layer III is directly vapourized, to get the maximum extent of heat consumption; (2) the volume expansion of W matrix is ignored; (3) the melt layer motion is disregarded. For a melt cell with exposed surface of $100\,\mu\mathrm{m} \times 100\,\mu\mathrm{m}$, and thickness of $110\,\mu\mathrm{m}$, the latent heat of La_2O_3 vapourization is $\Delta H_1' = 1.16 \times 10^{-3}$ J. The gaseous products (LaO and O_2) heated from 2300 K, the temperature they are formed, to 3695 K, the temperature they escape out, contain the energy of $Q_g' = 6.65 \times 10^{-5}$ J. That is to say, the cooling effect can consume $Q_{La_2O_3'} = 1.23 \times 10^{-3}$ J, which however is quite inappreciable compared with the incident energy accumulated during the melting duration (0.3 s) $Q_1' = 6.9 \times 10^{-2}$ J.

Based on the above discussion, we propose the cleaning effect is the key mechanism for the suppression of cavitation. Assuming that the La-gases in layer III are exhausted, the temperature tends to increase and the region of layer III expands towards layer II where is rich in La_2O_3. Additional La_2O_3 will be involved in the cleaning effect. Thus, the impurity level in layer III stably keeps very low and W boiling can be effectually hampered. On the basis of this cleaning mode, we assume that W boiling is still possible to be avoided in the context of much severe or repeated heat loads as long as the doped La_2O_3 is not thoroughly exhausted. Further experiments for validating the suppression of cavitation in WL10 under multiple heat loads is ongoing. In addition, since La_2O_3 is the key contributor to the suppression of cavitation in the melted W, we think the fabrication route would little affect its efficacy. It is however still worth to conduct melting tests on different grades of W-La_2O_3, i.e. produced by other fabrication methods and with different contents of La_2O_3.

WL10 has been proved to have advantages in comparison with W: enhanced ductility which can decrease the costs for

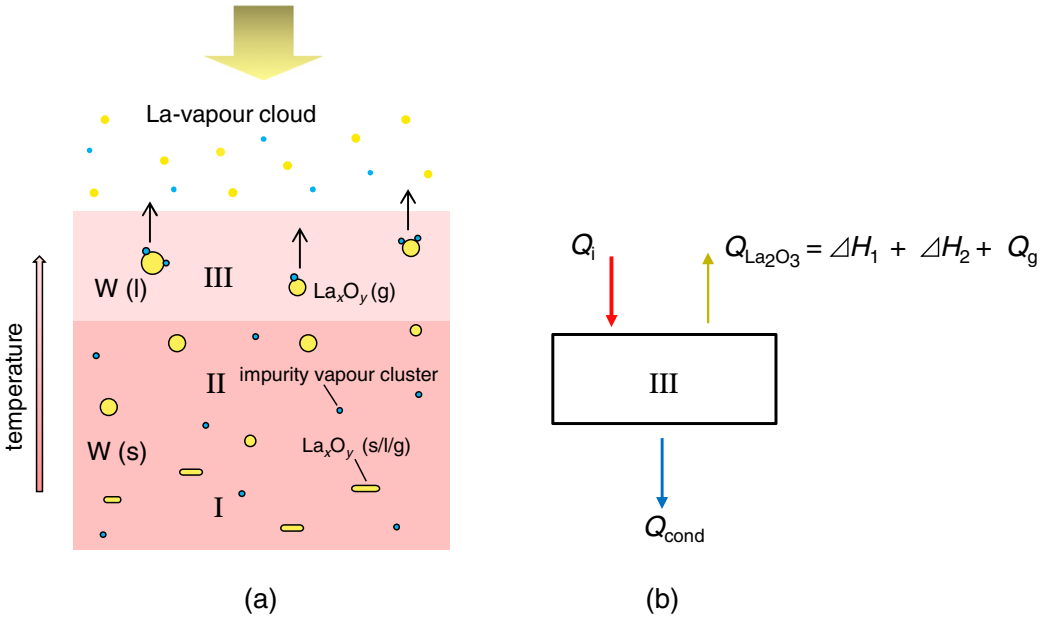

Figure 10. (*a*) Schematic presentation of the melting behaviour of WL10 under HHF load, and hereinto, La_xO_y ($(x, y) = (1, 1); (2, 3)$). (*b*) Simple diagram of the cooling effect in the top layer III, where Q_i is the incident heat, $Q_{La_2O_3}$ the energy consumption due to La_2O_3, and Q_{cond} the energy output towards the bulk by thermal conduction.

machining; higher recrystallization temperature; good thermal shock and creep resistance at elevated temperatures; etc. [16]. The results in this study suggest that WL10 has a better performance compared to CPW under melting exposure taking the cavitation issues into account. Since W cavitation is effectively suppressed in WL10, the tungsten sources (vapour and droplets), a terrible contaminant of plasma in the actual operations, can be significantly reduced [9], and furthermore, much denser resolidified material can be obtained which is conducive for the further performance. Considering melt ejection, an important issue for plasma operation, bubble boiling is not the sole contributor. In a fusion device, melt layer instability induced by intense plasma impact ($>10^3$ Pa) and Lorentz forces are also able to result in splashing of melt layers [5, 26, 34, 35]. La_3O_3 may change the properties of tungsten melt, e.g. surface tension and viscosity, which are important determinants of the melt instability [34–36]. Therefore, it is a strong need to comprehensively evaluate the application of lanthanum doped tungsten as PFM under high heat loads in fusion devices.

5. Conclusion

The focus of this work is on understanding the physics processes and underlying mechanisms involved in the cavitation issues for tungsten materials under heat loads. CPW and WL10 are exposed to HHF load for melting in GLADIS, and simultaneously, molybdenum plates are used as vapour collectors. Melt layer of the two tungsten grades are analysed with different techniques in order to study the structural evolutions. A lot of spherical voids are observed in the CPW resolidified layer. The size of the voids widely ranges from a clearly visible size to beyond 100 μm. They intensively distributed in the resolidified layer, and significantly increase the porosity to ~8.6% which implies the degradation of material. Around the open voids on the surface, deposited droplets can be seen clearly. These phenomena are attributable to the boiling of volume bubbles and their subsequent burst on the melt surface, as well as the accompanying melt layer ejection during CPW melting. On the contrary, for WL10, cavitation is inhibited and compact resolidified layer is obtained after melting exposure. In this compact resolidified layer, the content of La_2O_3 is dramatically reduced, suggesting its vapourization and escape. Subsidiary analyses on the components of vapour deposits show that, W vapourization is quite intense for CPW and gets much milder for WL10. Therefore, we conclude that cavitation in CPW is essentially due to the boiling of tungsten melt itself, and the impurities, which can act as heterogeneous nucleation sites, are able to reduce the required nucleation superheat and thus facilitate the melt boiling. We ascribe the suppression of cavitation in lanthanum doped tungsten to the reduced boiling of tungsten melt, which benefits from the decrease of the bubble nuclei due to the enhanced escape of the impurities with the active La-gas bubbles.

The presented results advance the current understanding of the mechanisms of cavitation in pure tungsten and its suppression in lanthanum doped tungsten. From the point of view of future material selection and development, it is very important and necessary to further investigate the application of lanthanum doped tungsten as a PFM in fusion devices, in view of the material erosion as well as the corresponding plasma performance.

Acknowledgments

The authors would like to thank Dr. H. Maier, Dr. K. Krieger, Prof. C. Linsmeier and Prof. Z.W. Zhou for the valuable discussions. This work was supported by National Magnetic Confinement Fusion Science Program of China under Grant 2013GB109004 and the Joint Sino-German research project GZ 763.

References

[1] Hirai T., Ezato K. and Majerus P. 2005 ITER relevant high heat flux testing on plasma facing surfaces *Mater. Trans.* **46** 412–24

[2] Pitts R.A. *et al* 2011 Physics basis and design of ITER plasma-facing components *J. Nucl. Mater.* **415** 957–64

[3] Neu R.L. 2010 Experience with high-Z plasma-facing materials and extrapolation to future devices *IEEE Trans. Plasma Sci.* **38** 453–60

[4] Garkusha I.E., Makhlaj V.A., Chebotarev V.V., Landman I., Tereshin V.I., Aksenov N.N. and Bandura A.N. 2009 Experimental study of plasma energy transfer and material erosion under ELM-like heat loads *J. Nucl. Mater.* **390–391** 814–7

[5] Bazylev B., Janeschitz G., Landman I., Loarte A., Klimov N.S., Podkovyrovd V.L. and Safronov V.M. 2009 Experimental and theoretical investigation of droplet emission from tungsten melt layer *Fusion Eng. Des.* **84** 441–5

[6] Sergienko G. *et al* 2007 Erosion of a tungsten limiter under high heat flux in TEXTOR *J. Nucl. Mater.* **363–365** 96–100

[7] Coenen J.W. *et al* 2011 Analysis of tungsten melt-layer motion and splashing under tokamak conditions at TEXTOR *Nucl. Fusion* **51** 083008

[8] Coenen J.W. *et al* 2011 Melt-layer ejection and material changes of three different tungsten materials under high heat-flux conditions in the tokamak edge plasma of TEXTOR *Nucl. Fusion* **51** 113020

[9] Philipps V. 2011 Tungsten as material for plasma-facing components in fusion devices *J. Nucl. Mater.* **415** S2–9

[10] Tokar M.Z., Coenen J.W., Philipps V., Ueda Y. and The TEXTOR Team 2012 Tokamak plasma response to droplet spraying from melted plasma-facing components *Nucl. Fusion* **52** 013013

[11] Hassanein A., Belan V., Konkashbaev I., Nikandrov L., Safronov V., Zhitlukhin A. and Litunovsky V. 1997 Modeling and simulation of melt-layer erosion during a plasma disruption *J. Nucl. Mater.* **241–243** 288–93

[12] Shi Y., Miloshevsky G. and Hassanein A. 2011 Boiling induced macroscopic erosion of plasma facing components in fusion devices *Fusion Eng. Des.* **86** 155–62

[13] Yuan Y., Greuner H., Boeswirth B., Luo G.-N., Xu H.Y., Fu B.Q. and Liu W. 2013 Melt layer erosion of pure and lanthanum doped tungsten under VDE-like high heat flux loads *J. Nucl. Mater.* **438** S229–32

[14] Nakamura K., Suzuki S., Tanabe T., Dairaku M, Yokoyama K and Akiba M. 1998 Disruption erosions of various kinds of tungsten *Fusion Eng. Des.* **39–40** 295–301

[15] Rieth M. *et al* 2011 Review on the EFDA programme on tungsten materials technology and science *J. Nucl. Mater.* **417** 463–7

[16] Smid I., Akiba M., Vieider G. and Ploechl L. 1998 Development of tungsten armor and bonding to copper for plasma-interactive components *J. Nucl. Mater.* **258–263** 160–72

[17] Ghezzi F., Zani M., Magni S., Vanacore G.M. and Tagliaferri A. 2009 Surface and bulk modification of W–La_2O_3 armor mock-up *J. Nucl. Mater.* **393** 522–6

[18] Taniguchi M., Nakamura K., Sato K., Ezato K., Yokoyama K. and Akiba M. 2001 Disruption erosion tests on La_2O_3 containing tungsten material *Fusion Technol.* **39** 890–3

[19] Linke J., Hirai T., Rodig M. and Singheiser L. 2004 Performance of plasma-facing materials under intense thermal loads in tokamak and stellarators *Fusion Sci. Technol.* **46** 142–51

[20] Greuner H., Boeswirth B., Boscary J. and McNeely P. 2007 High heat flux facility GLADIS: operational characteristics and results of W7-X pre-series target tests *J. Nucl. Mater.* **367–370** 1444–8

[21] Yuan Y., Greuner H., Boeswirth B., Krieger K., Luo G.-N., Xu H.Y., Fu B.Q., Li M. and Liu W. 2012 Recrystallization and grain growth behavior of rolled tungsten under VDE-like short pulse high heat flux loads *J. Nucl. Mater.* **433** 523–30

[22] Stralen S.V. and Cole R. 1979 *Boiling Phenomena: Physicochemical and Engineering Fundamentals and Applications* (Washington: Hemisphere)

[23] Newitt D.M., Dombrowski N. and Knelman F.H. 1954 Liquid entrainment 1: the mechanism of drop formation from gas or vapor bubbles *Trans. Inst. Chem. Eng.* **32** 244–61

[24] Worthington A.M. 1883 On impact with a liquid surface *Proc. R. Soc. Lond.* **34** 217–30

[25] Matthews J.W. (ed) 1975 *Epitaxial Growth* (New York: Academic)

[26] Coenen J.W. *et al* 2011 Tungsten melt layer motion and splashing on castellated tungsten surfaces at the tokamak TEXTOR *J. Nucl. Mater.* **415** S78–82

[27] v. Ardenne M. 1964 *Tabellen zur angewandten Physik, Bd. II* (Berlin: VEB Deutscher Verlag der Wissenschaften)

[28] De Temmerman G., Daniels J., Bystrov K., Berg M.A. and Zielinski J.J 2013 Melt-layer motion and droplet ejection under divertor-relevant plasma conditions *Nucl. Fusion* **53** 023008

[29] Stralen V. and Cole R. 1979 *Boiling Phenomena* (Washington: Hemisphere)

[30] Goldstein H.W., Walsh P.N. and White D. 1961 Rare earths: I. Vaporization of La_2O_3 and Nd_2O_3: dissociation energies of gaseous LaO and NdO *J. Phys. Chem.* **65** 1400–4

[31] Grundy A.N., Hallstedt B. and Gauckler L.J. 2001 Thermodynamic assessment of the lanthanum–oxygen system *J. Phase Equilib.* **22** 105–13

[32] Du Y., Yashima M., Koura T., Kakihana M. and Yoshimura M. 1995 Thermodynamic assessment of the ZrO_2–$LaO_{1.5}$ system *J. Eur. Ceram. Soc.* **15** 503–11

[33] *ITER Material Properties Handbook* 2001

[34] Miloshevsky G.V. and Hassanein A. 2010 Modelling of Kelvin–Helmholtz instability and splashing of melt layers from plasma-facing components in tokamaks under plasma impact *Nucl. Fusion* **50** 115005

[35] Shi Y., Miloshevsky G. and Hassanein A. 2011 Theoretical studies of macroscopic erosion mechanisms of melt layers developed on plasma facing components *J. Nucl. Mater.* **412** 123–8

[36] Zhang R., He X., Doolen G. and Chen S. 2001 Surface tension effects on two-dimensional two-phase Kelvin–Helmholtz instabilities *Adv. Water Res.* **24** 461–78